Linear Fluctuation Growth during Frontogenesis

JAMES C. MCWILLIAMS AND M. J. MOLEMAKER

Institute of Geophysics and Planetary Physics, University of California, Los Angeles, Los Angeles, California

E. I. OLAFSDOTTIR

University of Iceland, Reykjavik, Iceland

ABSTRACT

Near-surface, two-dimensional (2D) baroclinic frontogenesis induced by a barotropic deformation flow enhances the growth of three-dimensional (3D) fluctuations that occur on an ever smaller scale as the front progressively sharpens. The 3D fluctuation growth rate further increases with a larger deformation rate. The fluctuations grow by a combination of baroclinic and barotropic energy conversions from the 2D frontal flow, with the former dominating for most of the situations examined, ranging from small to $\mathcal{O}(1)$ values of the Rossby and Froude numbers and nondimensional deformation rate. Averaged 3D fluctuation buoyancy fluxes resist the 2D frontogenesis by a frontolytic tendency. They also augment the buoyancy restratification and potential-to-kinetic energy conversion tendencies of the 2D frontogenesis itself, and the 2D frontogenetic and 3D eddy-induced secondary circulations are mostly reinforcing (unlike in turbulent baroclinic jets). This shows that frontal instability coexists with, and potentially may even overcome, active frontogenesis; this conclusion is contrary to some previous studies. Frontal instability thus can augment frontogenesis in accomplishing a forward cascade of energy from oceanic mesoscale eddies into the submesoscale regime *en route* to finescale dissipation.

1. Introduction

Frontal patterns in temperature and velocity have long been recognized as common occurrences, especially near the surface in the lower atmosphere or upper ocean. In the atmosphere fronts are central features in synoptic-scale wintertime storms, and the so-called Bergen School based an early conceptual model with an intimate relation between a cyclone and its fronts (Bjerknes 1919). Later it was understood that winter storms arise primarily from the baroclinic instability of the planetary-scale westerly winds, but they nevertheless typically develop subsynoptic-scale fronts through the frontogenetic effect of a synoptic-scale deformation flow [i.e., with a nonzero horizontal strain rate, Bergeron (1928)]. In the ocean, surface fronts are also common, both as quasi-permanent features of the general circulation (e.g., in the Antarctic Circumpolar Current) as well as

more ephemeral but abundant, densely packed, submesoscale structures that are evident in satellite surface temperature images (Castelao et al. 2006; Ullman et al. 2007).

Surface-intensified, submesoscale frontogenesis caused by a mesoscale straining deformation field is an active process in simulations of several turbulent rotating, stratified flow regimes (Capet et al. 2008; Molemaker et al. 2009). The essential dynamics of surface frontogenesis in these turbulent simulations appears to be generally consistent with the model of Hoskins and Bretherton (1972) [also see the general theoretical summary in Hoskins (1982)]. Additionally, in these simulations three-dimensional (3D) fluctuations sometimes grow vigorously on the front, although the circumstances and mechanisms for their growth are presently unclear. Flament et al. (1985) gives an observational example of an oceanic, horizontally meandering, submesoscale, frontal instability.

If the deformation rate α were zero and the frontal flow steady (e.g., hydrostatic, geostrophic, and inviscid), then this situation could be analyzed as a familiar type of linear instability process, where baroclinic, barotropic,

Corresponding author address: James C. McWilliams, IGPP, UCLA, Los Angeles, CA 90095-1567.
E-mail: jcm@atmos.ucla.edu
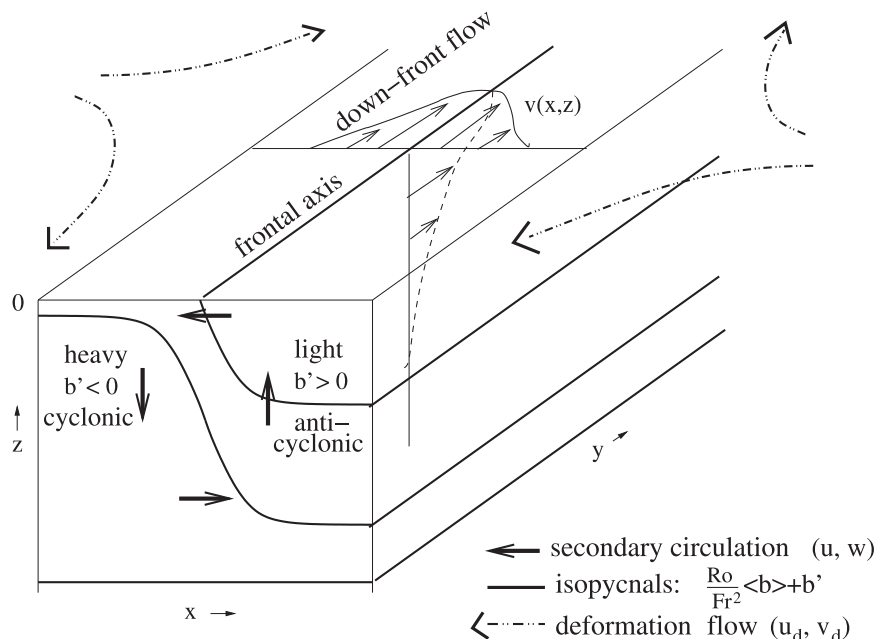
FIG. 1. Flow configuration for surface baroclinic frontogenesis induced by a barotropic deformation flow.

and—at larger Rossby number Ro—ageostrophic and centrifugal instability modes each might occur for various flow configurations. There is extensive literature on the linear instability of stationary frontal flows in the absence of deformation (e.g., Schär and Davies 1990; Barth 1994). However, when the deformation field is present and the frontal flow is intensifying, there is no general theoretical framework for analyzing frontal fluctuation growth. An analogy is sometimes suggested for a vorticity filament (i.e., a thin shear layer) in a barotropic fluid. Without deformation the flow is barotropically unstable. With a uniform deformation field oriented to narrow progressively the shear-layer width, the layer is stabilized (Dritschel et al. 1991). By this analogy one expects deformation to suppress the frontal fluctuation growth; hence, frontogenesis would be antithetical to frontal instability. Furthermore, in Eady's flow [with uniform potential vorticity between two vertical boundaries; i.e., Eady (1949)], the growth of baroclinic instability is suppressed by active deformation (Bishop 1993), further suggesting that frontogenesis limits frontal instability even in a baroclinic fluid.

In this paper we show that this expectation is false for baroclinic frontogenesis by demonstrating that surface frontogenesis manifests an exponentially growing fluctuation mode even in the presence of active deformation. Furthermore, the fluctuation growth rate is strongly amplified by frontogenesis that causes rapidly increasing Ro and Froude number (Fr) values for the frontal flow. This

growing fluctuation mode is a continuation of the dominant, geostrophic, normal-mode instability that occurs for a stationary frontal flow in the absence of deformation.

Spall (1997) numerically simulates a surface, baroclinic, mesoscale frontal flow in a deformation field that exhibits baroclinic instability and finite-amplitude equilibration as long as the deformation rate is weak enough and Ro and Fr are not too large. He interprets the latter limitation as consistent with the Bishop (1993) deformation–stabilization model. Our linear analysis supports both the importance of baroclinic instability and the frontogenetic equilibration tendency induced by the growing mode (although we do not examine the nonlinear equilibration process). However, we do not find evidence for frontal stabilization with large α, Ro, and Fr; in fact, we find that frontal instability is enhanced by increases in each of these parameters. This discrepancy is further addressed in section 9.

2. Governing equations and parameters

We first pose an idealized problem for two-dimensional (2D), baroclinic, upper-surface frontogenesis induced by a barotropic deformation flow $\mathbf{u}_d$ with a deformation rate $\alpha(t)$ (equal to half the rate of strain):

$$u_d = -\alpha x, \quad v_d = \alpha y, \quad w_d = 0. \quad (1)$$

The configuration for the problem is sketched in Fig. 1, including the secondary circulation that arises in the

frontal plane. This deformation flow has no vorticity, no horizontal divergence, and no associated buoyancy variation even in the presence of a background vertical stratification. The deformation flow is conducive to frontogenesis with a frontal axis aligned with $\hat{\mathbf{y}}$. We take the view that $\mathbf{u}_d$ arises from flow dynamics controlled remotely away from the frontogenetic region and is externally specified in the problems we solve. For example, a time-varying vorticity field with compact support and finite circulation has a far-field velocity that is dominated by strain and can be locally Taylor expanded about the frontal location, $(x, y) = 0$, as a dynamically inconsequential uniform velocity plus the shear flow in (1).

We define the total flow as $\mathbf{u} + \mathbf{u}_d$. Substituting this flow into the incompressible Boussinesq equations and discarding terms independent of $\mathbf{u}$ (considered part of the deformation field dynamics) yields interaction terms in the advection operator $\propto \mathbf{u}_d$; hence, $\propto (x, y)$. These terms are computationally awkward to deal with in a large but finite horizontal domain centered around the front, so we make a coordinate transformation moving with the deformation flow (1) that eliminates these secular terms from the advection operator (and has the further benefit of preserving better spatial resolution during frontogenesis than do fixed coordinates):

$$X = xe^{\beta}, \quad Y = ye^{-\beta}, \tag{2}$$

with $\beta = \int_o^t \alpha(t)\, dt$ (cf. Hoskins and Bretherton 1972). To a first approximation (as shown in section 4), frontogenesis sharpens the x gradients in $\mathbf{u}$ while nearly preserving the structure in X. Often there is a similar sharpening of the vertical gradients; therefore, for computational accuracy we further define a transformed vertical coordinate:

$$Z = ze^{\beta_z}, \tag{3}$$

with $\beta_z = \int_o^t \alpha_z(t)\, dt$. In all the solutions analyzed in this paper, we choose $\alpha_z(t) = \alpha(t)$. The important physical boundary is the top surface at $z = Z = 0$. Finally, the time coordinate is unchanged in the transformation, $T = t$. The solutions considered below have a specified Y structure and have vanishing flow speeds as $|X|, |Z| \to \infty$.

The ideal 3D Boussinesq equations are nondimensionalized with the following scales:

$$\begin{aligned} (X, Y) &\sim l, \quad Z \sim h, \quad v \sim V, \\ u &\sim U, \quad w \sim \frac{Uh}{\ell}, \quad T \sim \frac{l}{U}, \\ \varphi &\sim fVl, \quad b \sim \frac{flV}{h}, \quad \alpha \sim \frac{U}{l}. \end{aligned} \tag{4}$$

Both V and Y are oriented along the frontal flow, and U and X are across it; Z and w are vertical components; φ is the pressure normalized by mean density ρ_o; and $b = -g\rho/\rho_o$ is the buoyancy field. Nondimensional parameters are

$$\mathrm{Ro} = \frac{V}{f\ell}, \quad \mathrm{Fr} = \frac{V}{Nh}, \quad \lambda = \frac{h}{l}, \quad \varepsilon = \frac{U}{V}. \tag{5}$$

Here f is the Coriolis frequency assumed to be spatially uniform, and N is the buoyancy frequency assumed to approach a constant at depth. For an incipient oceanic front all of the parameters in (5) typically have small values for mesoscale currents, and in this paper we assign them nominal values[1] of $\mathrm{Ro} = \mathrm{Fr} = \varepsilon = 0.1$ and $\lambda = 0.01$. These imply that the frontal flow will be approximately geostrophic and hydrostatic, at least before the deformation flow causes significant frontogenesis.

In (X, Z, T) coordinates the nondimensional, inviscid, 2D frontal equations are

$$\begin{aligned} \varepsilon^2 \mathrm{Ro} D_\perp u - v + e^{\beta}\varphi_X &= \varepsilon^2 \mathrm{Ro}\,\alpha u, \\ \mathrm{Ro} D_\perp v + u &= -\mathrm{Ro}\,\alpha v, \\ \varepsilon^2 \lambda^2 \mathrm{Ro} D_\perp w - b + e^{\beta_z}\varphi_Z &= 0, \\ D_\perp b &= 0, \\ e^{\beta} u_X + e^{\beta_z} w_Z &= 0. \end{aligned} \tag{6}$$

The full buoyancy field is the sum of the background stratification $\langle b \rangle(z)$ and its frontal deviation:

$$b = \frac{\mathrm{Ro}}{\mathrm{Fr}^2}\langle b \rangle + b'. \tag{7}$$

The 2D substantial time derivative is

$$D_\perp = \partial_T + e^{\beta} u \partial_X + e^{\beta_z} w \partial_Z + \alpha_z Z \partial_Z. \tag{8}$$

We further consider 3D fluctuations whose dynamics are linearized about the preceding 2D frontal flow. Another advantage of the coordinate transformation is that a separable solution form exists for the alongfront direction when $\alpha \neq 0$; for example, the fluctuation cross-front velocity in complex notation is represented as $\hat{u}(X, Z, T)e^{ikY}$. The nondimensional fluctuation amplitudes are solutions of the following PDE system:

---

[1] Dimensional scales consistent with these values are the following: $f = 10^{-4}$ s^{-1}, $N = 10^{-2}$ s^{-1}, $l = 10$ km, $h = 100$ m, $V = 0.1$ m s^{-1}, and $U = 0.01$ m s^{-1}.

$$\varepsilon^2 \text{Ro}(D_\perp \hat{u} + e^\beta u_X \hat{u} + e^{\beta_z} u_Z \hat{w}) + ik\varepsilon \text{Ro} e^{-\beta} v\hat{u} - \hat{v} + e^\beta \hat{\varphi}_X = \varepsilon^2 \text{Ro}\alpha\hat{u},$$

$$\text{Ro}(D_\perp \hat{v} + e^\beta v_X \hat{u} + e^{\beta_z} v_Z \hat{w}) + \left(\frac{ik}{\varepsilon}\right)\text{Ro} e^{-\beta} v\hat{v} + \hat{u} + \left(\frac{ik}{\varepsilon}\right)e^{-\beta}\hat{\varphi} = -\text{Ro}\alpha\hat{v},$$

$$\varepsilon^2 \lambda^2 \text{Ro}(D_\perp \hat{w} + e^\beta w_X \hat{u} + e^{\beta_z} w_Z \hat{w}) + ik\varepsilon\lambda^2 \text{Ro} e^{-\beta} v\hat{w} - \hat{b} + e^{\beta_z}\hat{\varphi}_Z = 0, \qquad (9)$$

$$(D_\perp \hat{b} + e^\beta b_X \hat{u} + e^{\beta_z} b_Z \hat{w}) + \left(\frac{ik}{\varepsilon}\right)e^{-\beta} v\hat{b} = 0,$$

$$e^\beta \hat{u}_X + \left(\frac{ik}{\varepsilon}\right)e^{-\beta}\hat{v} + e^{\beta_z}\hat{w}_Z = 0.$$

In this paper we do not include nonlinear fluctuation advection effects in integrating either (6) or (9), but we do analyze the emerging averaged fluctuation buoyancy flux divergence in section 6.

3. Computational method

The code uses staggered-grid, finite-difference discretization in space for (6)–(9), and a third-order Adams–Bashforth scheme is used to advance the variables in time. It uses a QUICK algorithm for the advection of velocities and scalars, and a multigrid Poisson solver for determination of φ and $\hat{\varphi}$ within each time step. These methods have been successfully used before (Molemaker and Dijkstra 2000; Molemaker et al. 2009).

The model equations have anisotropic viscous and buoyancy diffusion terms, partly for discretization noise control. In the results presented below, they have negligible dynamical influence because of their small coefficients. The boundary conditions are zero-normal flow at $x = \pm L_x/2$ and $z = -L_z, 0$. Viscous and diffusive terms at near-boundary grid points are evaluated by extrapolation from adjacent interior grid values[2] [e.g., near $z = 0$, a ghost point is defined by $v(-dz/2) = 3v(dz/2) - 3v(3dz/2) + v(5dz/2)$]. This choice is made to avoid boundary layers and limit the boundary fluxes of stress, buoyancy, and potential vorticity. The latter in particular may be large during frontogenesis, even with zero stress and buoyancy flux; this can lead to symmetric frontal instability if the potential vorticity evolves to change its sign within the domain (Hoskins 1974). However, this regime is not examined in this paper; the solutions we present do not have large changes in their potential vorticity values, nor do they exhibit strong sensitivity to the particular representation for stress- and flux-free boundary conditions. The usual nondimensional domain size is $L_x = 8$

and $L_z = 2$, while the initial frontal scales are $\mathcal{O}(1)$ in each direction. We use the same boundary conditions in (X, Z). Except for $z = Z = 0$, these boundary conditions are artificial approximations to an unbounded domain as $(x, X) \to \pm\infty$ and $(z, Z) \to -\infty$. We stop the time integrations before the shrinking domain boundary (due to the deformation-flow coordinate transformation; see section 2) encroaches too severely on the region with significant frontal and fluctuation amplitudes. The solutions below are obtained with an (X, Z) grid size of $(128, 128)$, and we tested that similar solutions are found with larger grid size. Since frontogenesis has a super-exponential rate (section 4), we expect an ever stiffer grid-resolution requirement at later times; however, the solutions here are not integrated into a regime where our resolution becomes inadequate.

In the solutions in sections 4 and 5, a particular initial condition is used for the 2D fields. It has an initial alongfront flow $v(x, z)$ in geostrophic, hydrostatic balance with the buoyancy field $b(x, z)$, which has a uniform stratification away from the front:

$$v(x, z) = \frac{2}{\sqrt{\pi}} \exp[Az] \exp[-(Bx)^2],$$

$$b'(x, z) = \frac{A}{B} \exp[Az] \, \text{erf}[Bx], \qquad (10)$$

$$\langle b \rangle(z) = G(L_z + z),$$

$$u(x, z) = w(x, z) = 0.$$

Our standard parameter choices are $A = 3.0$, $B = 2.0$, and $G = 1.2$ (Fig. 3, top row). [Different initial conditions are examined in section 8, including some that have more of a surface mixed layer structure, at least in $\langle b \rangle(z)$.]

The Ertel potential vorticity associated with (6)–(8) is

$$\Pi = (1 + \text{Ro}\partial_x v)\left(\frac{\text{Ro}}{\text{Fr}^2}\partial_z \langle b \rangle + \partial_z b'\right) - \text{Ro}\partial_z v \partial_x b'.$$

With (10), Π exhibits reversals in both its vertical and horizontal gradients: the $v(x, z)$ profile implies cyclonic

---

[2] These boundary conditions are not accurately transmissive for outward radiation of inertia–gravity waves (cf. Klemp and Duran 1983), but we are careful to keep the generated wave amplitudes small in our solutions in the several ways described in this section.

relative vorticity for $x < 0$ and anticyclonic for $x > 0$, and the weak, near-surface vertical density stratification in the far field as $x \to -\infty$ reduces the potential vorticity (i.e., is anticyclonic relative to the spatial mean value), while the opposite far field has stronger stratification (i.e., is cyclonic). These sign-reversing lateral potential-vorticity gradients satisfy the Rayleigh necessary condition for geostrophic barotropic and baroclinic instabilities of a stationary, parallel flow. In the geophysical fluid literature this is often referred to as the Charney–Stern condition, which explicitly implicates the interior potential vorticity gradient $\partial_x \Pi$ and the boundary buoyancy gradient $\partial_x b'(x, 0)$ (Eliassen 1984). We show in section 5 that such 3D instabilities do occur with (10), both with and without active deformation α, and in section 8 we show that the character of the instability can shift from baroclinic to barotropic as the relative contributions of $\partial_z v$ and $\partial_x v$ change. In contrast, the special case frontogenetic problem with uniform potential vorticity, often adopted in the frontogenesis literature (e.g., Hoskins and Bretherton 1972), does not satisfy the Rayleigh necessary condition for linear instability in a semi-infinite domain (i.e., with one boundary, unlike Eady's flow with two boundaries), and thus this type of frontogenesis cannot manifest the essentially geostrophic instabilities that are the focus of this paper. The absence of linear frontal instability holds in particular for the stationary fronts in the small-Ro asymptotic model, surface quasigeostrophy (Held et al. 1995). Many previous instability studies have been made for variants of Eady's flow (Bishop 1993; Song and Nakamura 2000; Heifetz et al. 2004), but we view this two-boundary model as dubiously relevant to a single-boundary front, at least when its solution behavior is qualitatively different.

We consider this $v(x, z)$ profile as a representative balanced, surface, frontal flow. It is susceptible to both barotropic and baroclinic normal-mode instabilities for small Ro and Fr due to its combined horizontal and vertical shears. Abundant experience has shown that such flows are quantitatively sensitive to the details of their shear profiles. Our goal in this paper is to demonstrate what we found to be generic frontogenesis and fluctuation growth behavior under active deformation without exhaustively surveying the profile sensitivities.

The deformation field $\alpha(t)$ is initially zero but ramps up to an asymptotic dimensional value of α_0 over a non-dimensional time period of $\Delta t \approx 0.25$. Consequently, the cross-front flows are also initially zero: $u = w = 0$. The reason for a ramp up is to diminish early time generation of 2D inertia–gravity waves caused by deformation shock (Snyder et al. 1993). Our analyses in sections 4–8 are restricted to $t \geq \Delta t$ whenever $\alpha \neq 0$.

The 3D fluctuation equations are solved with spatially white, random noise as an initial condition[3] in $(\hat{u}, \hat{v}, \hat{w}, \hat{b})(x, z)$ and a specified value for the alongfront wavenumber k at time $t_0 \geq \Delta t$. The combined 2D–3D system is integrated forward in time until time t_1. At that point, the integration is restarted at $t = t_0 \leq t_1$ with the 2D solution reinstated at t_0, but the 3D fields at t_1 are reinterpreted as initial conditions at t_0. This is repeated as an iterative "breeding" procedure that allows the most rapidly growing fluctuation to emerge from the initial noise (cf. Toth and Kalnay 1997). It is important that the integration interval, $t_1 - t_0$, not be too large so that the fluctuations not be too disrupted by restarting at an earlier phase of the 2D flow and associated deforming grid. (A symptom of an excessively large interval is spurious excitation of inertia–gravity waves in the 3D fields by the restart.) In the results below, the interval is usually chosen as $t_1 - t_0 = 0.006\ 25$, and the number of breeding cycles is 800 with a total fluctuation breeding time interval of 5. This breeding procedure is nearly the same as freezing the 2D frontogenesis fields at t_0 while continuing to integrate the 3D fluctuations forward with nonzero α, which is justifiable a posteriori if the amplifying fluctuation exponential growth rate σ is much larger than the frontogenetic deformation rate α. A frozen-2D fluctuation formulation could be analyzed as a generalized eigenvalue problem; however, we can obtain essentially the same answer by doing breeding time integrations with a short $t_1 - t_0$, so we did not feel it was necessary to separately develop the eigenvalue method. If the resulting σ were smaller than α_0, then, insofar as the latter is a rough characterization of the 2D frontal rate of change (section 4), we should not expect the 3D fluctuation growth to be very accurate with either breeding or frozen-2D calculations since the frontal changes would alter the background state before the fluctuations changed. Solutions are presented with a consistent, simultaneous 2D and 3D evolution without this breeding approximation in section 7.

4. Two-dimensional frontogenesis

The essential phenomenology and dynamical understanding for 2D frontogenesis are well known, at least within the context of the assumptions of semigeostrophic

---

[3] Because the initial 3D fields are mutually uncorrelated (hence unbalanced), they quickly adjust from having equal amplitudes to having $\hat{u}$ and $\hat{w}$ that are $\mathcal{O}(\varepsilon^{-1})$ larger than $\hat{v}$ and $\hat{b}$ since they do not conform to the 2D frontal scaling assumed in section 2, as evident in Fig. 6. However, these relations are overtaken by the emergent, growing fluctuation mode(s) that are approximately balanced for $\hat{u}$ as well as $\hat{v}$.

balance and uniform potential vorticity in the interior (Hoskins 1982)—neither of which are assumed here, although this does not change the essential 2D results. A surface-intensified lateral buoyancy gradient and its associated geostrophic alongfront flow in the presence of a favorably aligned deformation flow (Fig. 1) has its cross-front lateral gradients sharpen with time and develops a closed, secondary circulation with an upward flow on the buoyant side and a surface horizontal flow across the front toward the dense side that further accelerates the frontal sharpening. With semigeostrophic balance and uniform potential vorticity, the front becomes infinitely thin in finite time (Hoskins and Bretherton 1972), but this singular behavior is a priori implausible even though proof of finite-time regularity is still a mathematically open question for fluid dynamical equations such as (6). Two-dimensional simulations have shown an increasingly unbalanced evolution as frontogenesis proceeds (Snyder et al. 1993). A heuristic rationalization of the rate of development of the secondary circulation comes from the x momentum equation in (6), assuming exact geostrophic balance for v and $\partial_x \varphi$ and neglecting advective nonlinearity:

$$\text{Ro}\varepsilon^2(\partial_t - \alpha)u \approx 0 \Rightarrow u \propto \exp(\beta);$$

that is, exponential amplification in time. Two-dimensional continuity requires that w amplify along with u (neglecting any evolving differences in their X and Z scales). A similar rationalization of frontal sharpening comes from assuming passive advection of the frontal fields by the deformation flow (1), which implies x gradients also grow $\propto \exp(\beta)$. The solutions below show that these heuristic estimates are qualitatively apt but quantitatively imprecise.

The expected behaviors are confirmed in our solutions. Here, we consider a standard case with the parameter values in section 2 and initial conditions in (10), together with a nondimensional deformation rate of $\alpha_0 = 1.0$. As time-evolving measures for the magnitude of the alongfront shears, we define local Rossby and Froude numbers by $\widetilde{\text{Ro}}(t) \equiv \text{Ro}(\max_{x,z}|\partial_x v|)$ and $\widetilde{\text{Fr}}(t) \equiv \text{Fr}(\partial_z \langle b \rangle)^{-1/2} \max_{x,z}|\partial_z v|$, respectively. Figure 2 shows that the frontal shears monotonically increase with time, indicating the occurrence of frontogenesis with decreasing cross-frontal and vertical scales. The functional form of the increase is approximately $\propto \exp(\beta)$. At times later than $t \approx 1$, their growth curves are convincingly superexponential, but accurate computations are increasingly difficult in a collapsing front, and in this paper we do not pursue the late time regime with large $\widetilde{\text{Ro}}$. (Other initial profiles sometimes show quantitatively different growth curves; e.g., see section 8.) Neverthe-
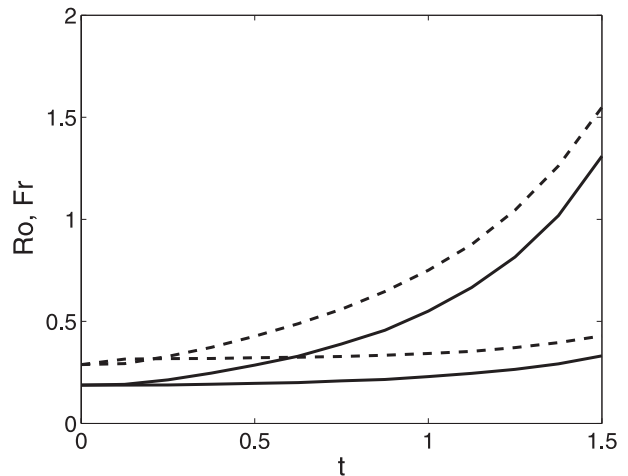

FIG. 2. Temporal growth of maximum local Rossby ($\widetilde{\text{Ro}}$; solid) and Froude ($\widetilde{\text{Fr}}$; dashed) numbers during 2D frontogenesis for $\alpha_0 = 1.0$ and the initial profile (10). The lower curves are normalized by e^β and e^{β_z}, respectively.

less, even over this limited period of frontogenesis up to $t = 1.5$, the Rossby and Froude numbers grow to $\mathcal{O}(1)$ values.

The 2D frontal fields are illustrated in Figs. 3–5. Both $v(x, z)$ and $b(x, z)$ remain approximately in thermal wind balance as their horizontal and vertical scales shrink. The frontal strength is measured by the square of the horizontal buoyancy gradient, $(\partial_x b)^2/2$, and steadily increases in magnitude with its maximum located at the surface and moving to the left with advection by $u(x, 0, t)$. The secondary circulation streamfunction ψ (with $u = \partial_z \psi, w = -\partial_x \psi$) spins up from zero to a counterclockwise flow in the (x, z) plane: upward on the light side and downward on the dense side, toward the dense side near the top surface and toward the light side at depth. The center of the front moves toward the dense side due to advection by this secondary circulation. The direction of this secondary circulation is to convert frontal potential energy into frontal kinetic energy since $wb' > 0$ on average. Similarly, this correlation implies that the secondary circulation acts to increase the stratification in the vicinity of the front; this is sometimes called restratification since it acts opposite to destratification by vertical buoyancy mixing.

The maximum in v shows only a moderate increase with time, while its gradients are growing approximately exponentially (Fig. 2). The magnitude of $\partial_x b$—whose square is often taken as a pointwise measure of frontal strength (section 6)—also grows approximately exponentially, and its spatial pattern shows horizontal and vertical scale contractions toward the moving frontal center at the surface (Fig. 4). The secondary circulation is expressed in the cross-front streamfunction field ψ
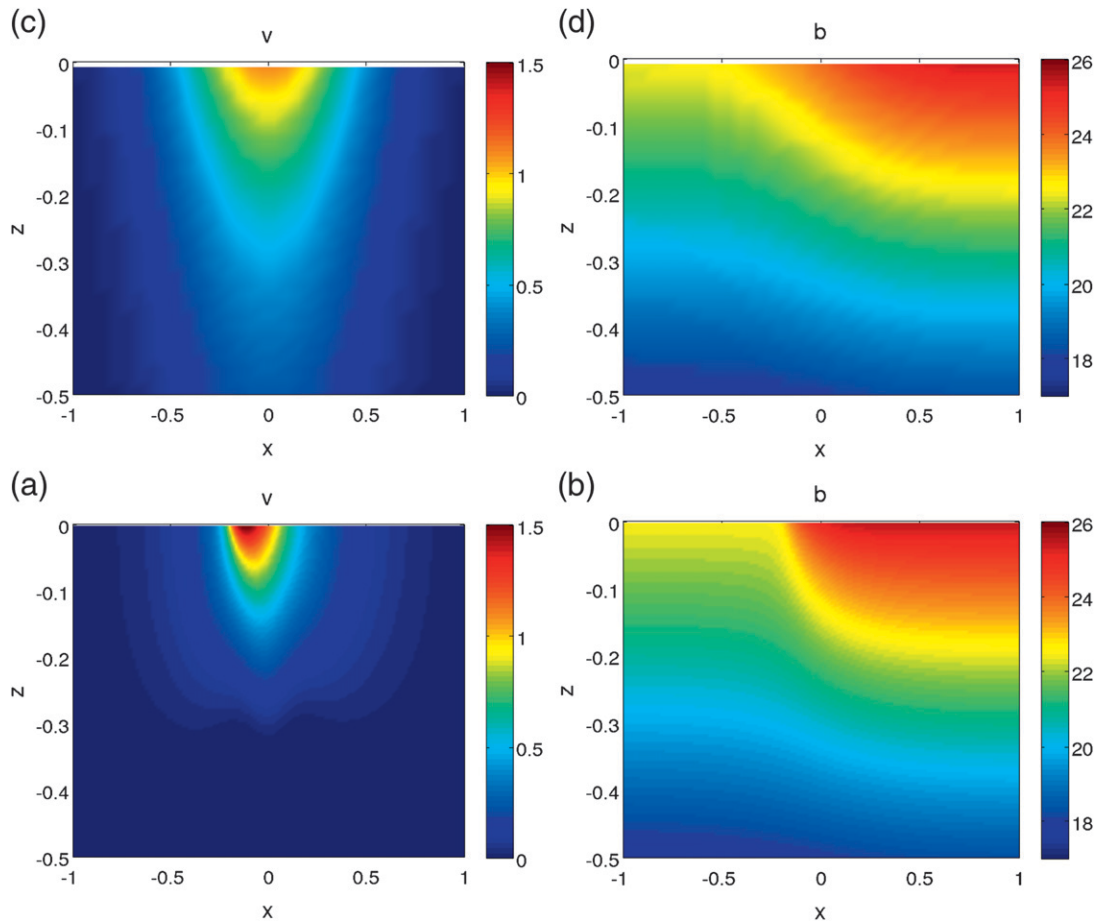
FIG. 3. The 2D frontal fields in the upper-central part of the (x, z) plane at (top) $t = 0.0$ and (bottom) $t = 1.5$ with $\alpha_0 = 1.0$: (left) v and (right) b.

(Fig. 5). It is initially zero because $\alpha(0) = 0$ (section 3), but it amplifies in magnitude early in frontogenesis as u and w increase; however, because the rate of scale contraction is ultimately stronger than the rate at which (u, w) increase, the amplitude of ψ peaks at $t \approx 0.3$ and thereafter declines during frontogenesis.

In the energy balance for the 2D frontal flow (cf. the appendix for the 3D fluctuation flow), there is an energy loss to the background deformation flow [i.e., $\alpha(\varepsilon^2 u^2 - v^2) < 0$ for small ε] and a conversion from frontal potential energy to kinetic energy (i.e., $wb' > 0$ for the secondary circulation in Fig. 5). In a diagnostic test of cross-front geostrophic, hydrostatic balance for the alongfront flow (i.e., $\partial_z v - \partial_x b$, normalized by the magnitude of either term alone), the deviations were found to grow during frontogenesis but never to exceed a few percent for the regime examined here, as long as the deformation field $\alpha(t)$ is slowly varying and does not excite inertia–gravity waves. The alongfront momentum balance, however, is ageostrophic to leading order; front-

ogenesis is an unbalanced process with respect to the secondary circulation it generates.

5. Three-dimensional fluctuation growth

Now consider the evolution of separable 3D fluctuations in (9). We first solve the stationary-front problem without deformation. This is done by choosing $t_0 = 0.0$. In this case the bred fluctuation is equivalent to the most unstable normal mode for each k value. For the initial frontal profile (10), the maximum 3D fluctuation growth occurs for $k_{max} = 2.0$. An exponential fit to the time history of fluctuation magnitudes (Fig. 6) is very accurate after an initial period of adjustment, indicating both the success of our breeding technique and the unimportance of 2D frontal evolution during the brief breeding interval. It shows a nondimensional growth rate of $\sigma_{max} = 2.00$. Thus, even at $t_0 = 0.0$ in our standard case of 2D frontogenesis (section 4), $\sigma_{max} > \alpha_0$, which is consistent with the necessary conditions for the fluctuation breeding
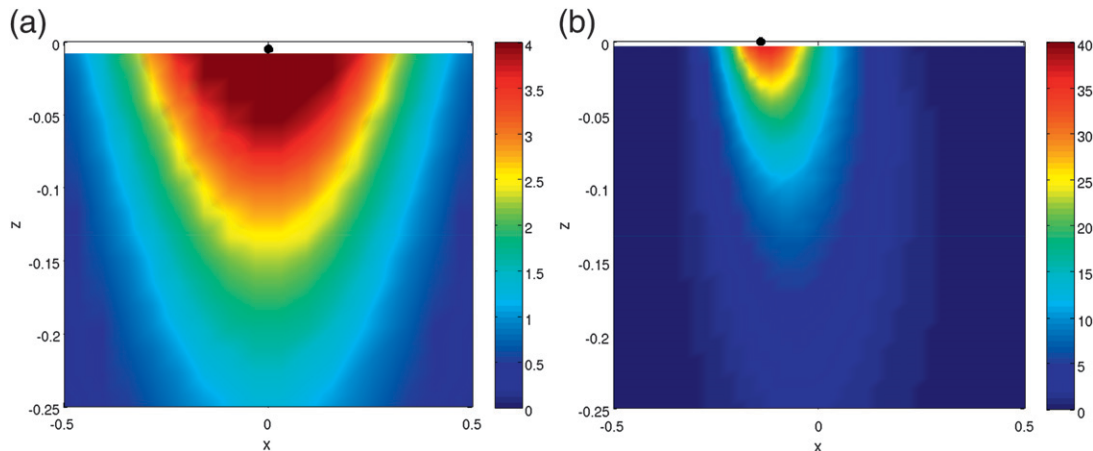
FIG. 4. The 2D frontal strength, $(\partial_x b)^2/2$, in the upper-central part of the (x, z) plane at (left) $t = 0.0$ and (right) $t = 1.0$ with $\alpha_0 = 1.0$. The dot denotes the position of maximum strength at this time. Note the different color scales; see section 6 for a frontogenetic dynamical balance analysis.

approximation (section 3). We will see that the accuracy of this approximation further improves with increasing t_0 since σ_{max} increases. The relation $\sigma_{max} > \alpha_0$ implies that 3D fluctuations grow faster than 2D gradients in frontogenesis (Fig. 2). This implies that perturbed fronts will usually manifest a 3D instability that becomes more evident as the 2D frontogenesis proceeds.

Since the growing 3D fields have complex coefficients multiplying e^{ikY} (section 2), we first show only the spatial patterns of their absolute values in Fig. 7. The larger modal magnitudes are in a horizontal and vertical region concentrated near the front except for $|\hat{w}|$, which reaches deeper into the interior. Notice that the magnitudes in $\hat{v}$ and $\hat{b}$ are comparable to each other (consistent with approximately geostrophic, hydrostatic balance in the cross-front momentum equation), while $|\hat{u}|$ is larger and $|\hat{w}|$ is smaller. A larger $|\hat{u}|$ indicates that the 2D frontal

scaling with $\varepsilon \ll 1$ does not apply to the 3D fluctuations. Its emerging magnitude, with nondimensional $|\hat{u}| \sim k\varepsilon^{-1}$, is consistent with an approximately geostrophic, hydrostatic balance in the alongfront momentum equation. The smaller $|\hat{w}|$ indicates that the fluctuation structure is dominated by meanders in the horizontal plane (Fig. 8), even though $\hat{w} \neq 0$ is essential to fluctuation growth by baroclinic energy conversion from the 2D frontal flow (see the appendix and Fig. 10). The largest $|\hat{v}|$ values are displaced from the frontal center at the cross-front edges of the meanders.

Because of the initially rather small values of Ro and Fr, we interpret this mode as approximately a quasigeostrophic instability. The energy balance analysis later in this section shows that the instability is a mixed type, with a baroclinic energy generation rate due to vertical shear $\partial_z v$ that is more than twice as large as the barotropic
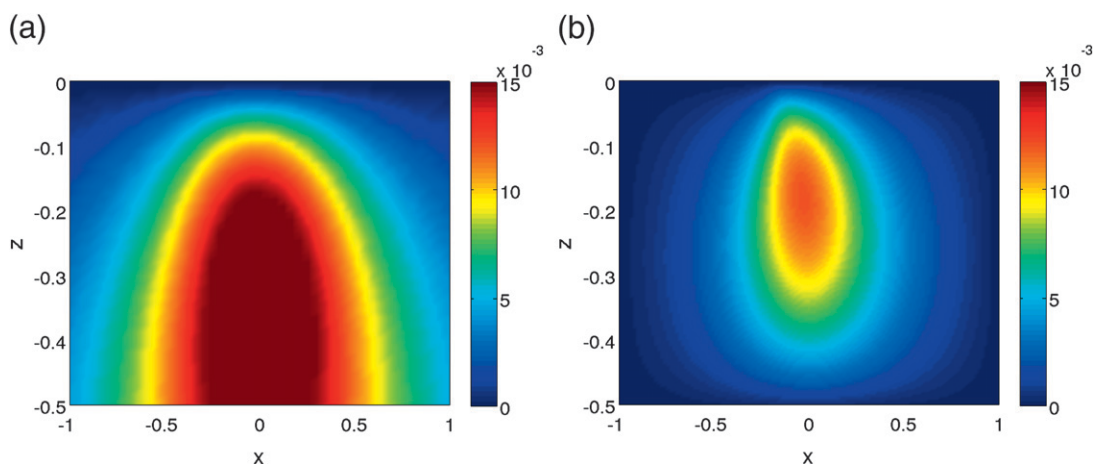

FIG. 5. The 2D secondary circulation streamfunction ψ (i.e., $u = \partial_z \psi$, $w = -\partial_x \psi$) for 2D frontogenesis at (left) $t = 0.5$ and (right) $t = 1.5$ with $\alpha_0 = 1.0$. The flow is upward on the right (anticyclonic, light) side of the front.
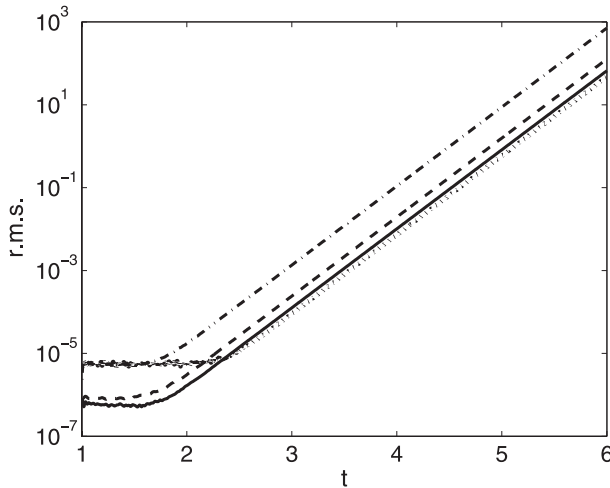
FIG. 6. Growth of rms 3D fluctuation amplitudes [e.g., $(\int \int e^{-\beta_z} |\hat{u}|^2 \, dX \, dY \, dZ)^{1/2}$] in a region centered around the 2D front for $\alpha_0 = 1.0$, $t_0 = 1.0$, $k = 9.5$ (the most rapidly growing mode for this case), and a breeding time interval of 5: $\hat{u}$ (dotted–dashed), $\hat{v}$ (solid), $\hat{w}$ (dotted), and $\hat{b}$ (dashed). Note the exponential growth with $\sigma = 4.39$.

generation rate due to $\partial_x v$. In this regime the most unstable wavenumber ($k = 2.0$) is approximately the same as both the inverse baroclinic deformation radius for the background stratification and the vertical scale of the frontal flow ($\mathrm{Fr}A/G\mathrm{Ro} = 2.5$ here, characteristic of baroclinic instability) and the inverse frontal width B [$=2$ here, characteristic of barotropic instability; e.g., McWilliams (2006)].

The experimental protocol for investigating the consequences of frontogenesis is to examine a succession of increasing t_0 values and at each one to make a survey in k values to identify the range in k where significant 3D fluctuation growth occurs and to identify its maximum growth rate, σ_{max} at k_{max}. Because the amplifying 3D fluctuations are bred over a given short time interval (section 3), this is essentially equivalent to freezing the 2D frontal fields in time and thus solving a normal-mode instability problem that exhibits temporal exponential growth with growth rate $\sigma > 0$. This is illustrated in Fig. 6 at $t_0 = 1.0$ for the fastest-growing mode with $k = k_{max}(t_0) = 9.5$ and in Fig. 9 for the unstable k range for several t_0. With our breeding procedure we are unable to identify modes with weak or no growth and, for any particular k, cannot find the unstable modes, if any, with weaker growth rates than the fastest-growing mode.

The emergent spatial patterns in $(\hat{u}, \hat{v}, \hat{w}, \hat{b})$ associated with the dominant mode at $t_0 = 1.0$ are shown in Fig. 7 (bottom). The 3D frontogenetic mode is somewhat similar in shape to the stationary-front instability mode except for its greatly reduced spatial scales in the cross-

front plane due to 2D frontogenetic scale contraction. In addition, there are some more subtle differences in the mode shape, such as the shift of its larger amplitude regions toward the dense side of the front approximately following the motion of the frontal center itself (Fig. 3). Figure 8 shows the horizontal phase structure of this mode in a horizontal plane near the top surface. The horizontal flow [rescaled to have a common dimensional horizontal velocity scale; i.e., nondimensional $(\varepsilon u, v)$] has recirculations around the $b'(x, y)$ extrema, consistent with geostrophic, hydrostatic balance. The vertical velocity $w(x, y)$ is fractionally displaced from $b'(x, y)$ in the upshear direction, consistent with baroclinic energy conversion from the 2D frontal flow to the 3D fluctuations (wb', $\mathcal{BF} > 0$; see the appendix).

We find that σ_{max} systematically increases with t_0, that is, with the frontal sharpening (Fig. 9 and Table 1). The associated alongfront wavenumber k_{max} as well as the bandwidth Δk for growing modes similarly increase. These results show that the horizontal scale of the instability is comparable to the frontal width with σ decreasing at both larger and smaller k values; this is familiar behavior from unstable stationary flows with both vertical and horizontal shear (Barth 1994). In a first approximation σ_{max} increases in pace with $\exp\beta$ (Table 1), similar to the rate of growth of the 2D shear magnitudes in the sharpening front (Fig. 2). The rates of increase in k_{max} and Δk are much faster than $\exp\beta$. This can be rationalized as a combination of an increase following the true shrinking 2D frontal scale and an increase to counter the artificial stretching associated with the transformed alongfront coordinate (n.b., $kY = ke^{\beta}y$); however, $k_{max}(t_0)$ in Table 1 does not increase quite as fast as $e^{2\beta(t_0)}$.

To further interpret the 3D fluctuation growth, we perform an energy balance analysis as defined in the appendix. Several of the associated fields are shown in Fig. 10 for both a stationary front ($t_0 = 0.0$) and actively sharpening frontogenesis ($t_0 = 1.5$). Again, we see qualitative similarity between the initial [$\alpha(0) = 0$] and frontogenetic [$\alpha(1.5) = \alpha_0$] stages. The fluctuation energy density $\mathcal{K} + \mathcal{A}$ is concentrated in the frontal zone (as expected from the modal patterns in Fig. 7), shrinking as the front sharpens. The integral conversion rates include the energy exchange with the deformation flow $\mathcal{DF}$, the conversion of fluctuation potential to kinetic energy $\mathcal{PK}$, and the energy conversions from the 2D frontal flow by both Reynolds stress $\mathcal{RF}$ and buoyancy flux $\mathcal{BF}$. Broadly over the domain all of these conversions are positive except for $\mathcal{DF}$, which is generally small but is sometimes negative (Table 1; n.b., negative conversion with the background deformation flow also occurs for the 2D frontal flow; see section 4). In Fig. 7 the buoyancy-flux
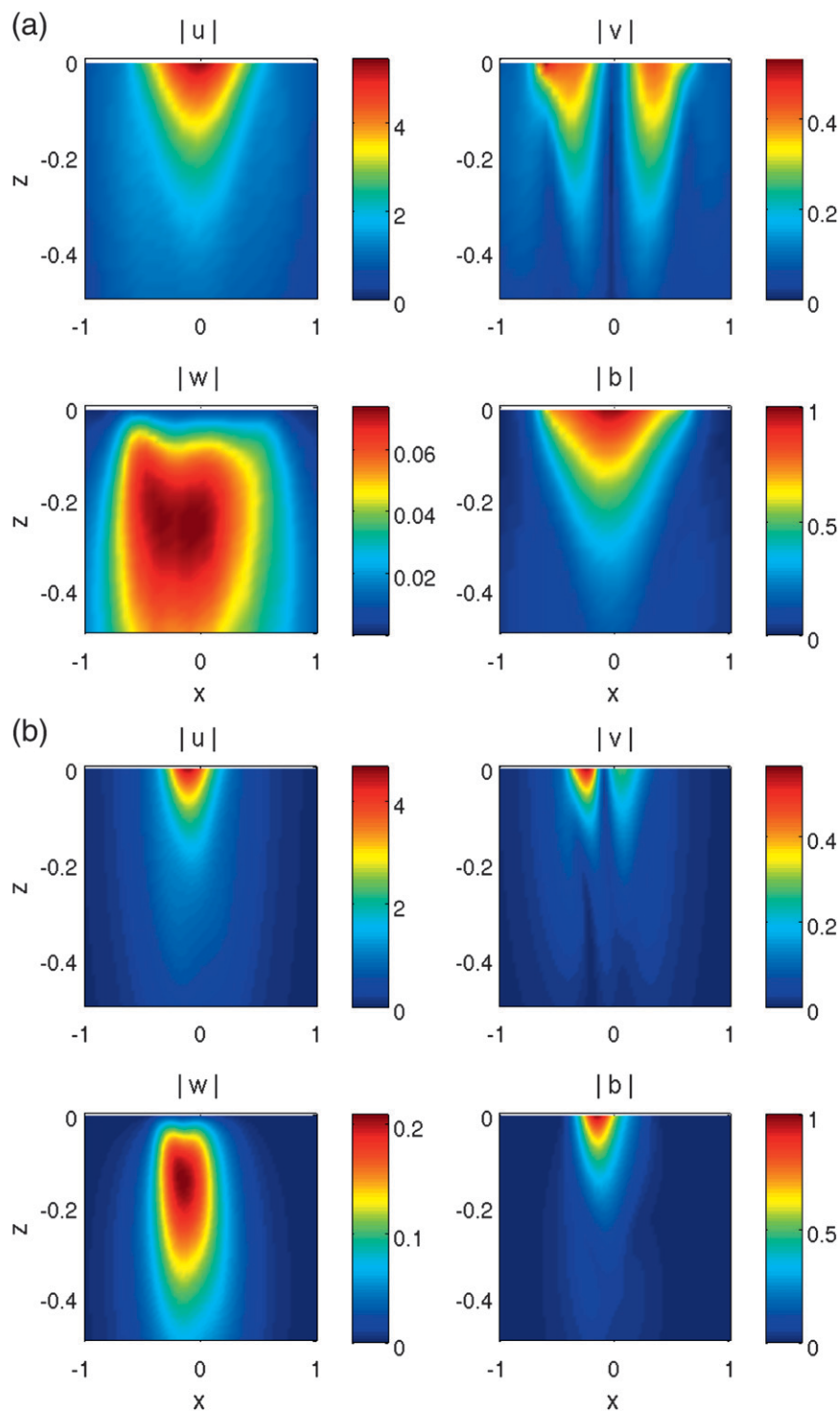
FIG. 7. Magnitudes of the complex 3D fluctuation fields in the upper-central part of the (x, z) plane for the fastest growing fluctuation modes at (top) $t_0 = 0.0$ (with $k = 2$) and (bottom) $t_0 = 1.0$ (with $k = 9.5$) with $\alpha_0 = 1.0$. The mode is normalized such that $\max_{x,z}|\hat{b}| = 1.0$.
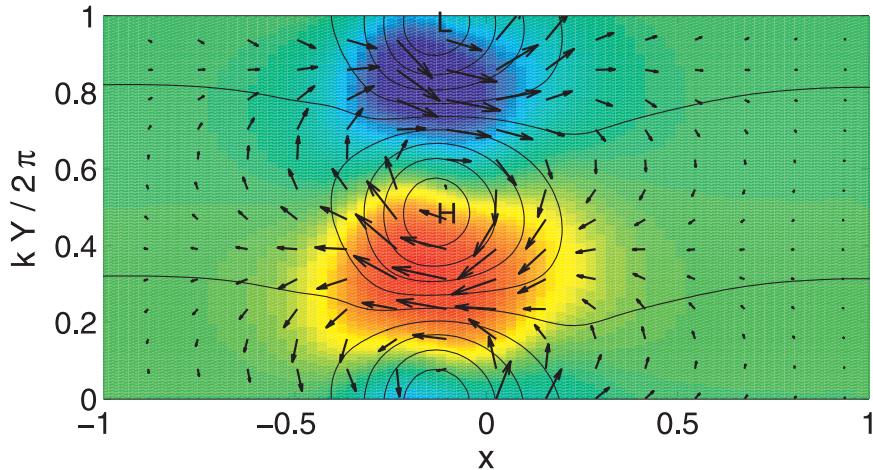
FIG. 8. The 3D fluctuation fields in the horizontal plane at $z = -0.16$ at $t_0 = 1.0$ for $\alpha_0 = 1.0$ and $k = 9.5$: $(\varepsilon u, v)$ as vectors, w in color (red upward), and b' with contours and H/L extremum labels.

conversion generation is concentrated in the frontal zone with approximately the same distribution as the vertical shear $\partial_z v$ and the frontal strength (Fig. 4; notice the different spatial domains in the plots). The Reynolds stress conversion is relatively weaker and is concentrated on the edges of the frontal flow where $|\partial_x v|$ is largest. On the cyclonic side $\mathcal{RF}$ is even locally negative near where $\partial_x v$ and $|\hat{v}|$ have maxima (Figs. 3 and 7); this feature becomes more pronounced in wider fronts where the instability becomes more purely baroclinic (section 8). The integrated conversion rates (normalized by the total fluctuation energy) for several t_0 values are listed in Table 1.

Baroclinic generation from the unstable front, $\mathcal{BF} > 0$, is the dominant source of fluctuation growth. Hence, we can identify this growing mode as a form of baroclinic instability (but also see section 8). Here $\mathcal{RF}$ is also positive for all t_0 values but not as a large as $\mathcal{BF}$. Although positive except for late-time frontogenesis, $\mathcal{DF}$ is much smaller. Hence, $\mathcal{PK} > 0$ to maintain the partition between $\mathcal{K} < \mathcal{A}$ in the baroclinically unstable mode. With increasing frontogenetic development (i.e., increasing t_0), the dominance of baroclinic energy generation increases. The primary frontal instability mechanism in Capet et al. (2008) was by baroclinic conversion.

A diagnostic test of geostrophic, hydrostatic balance for the fluctuations shows unbalanced deviations that grow with t_0 (hence with $\widetilde{\mathrm{Ro}}(t_0)$ and $\widetilde{\mathrm{Fr}}(t_0)$). The deviations reach a relative level of several tenths at the largest t_0 examined here, in contrast to the apparent origin as a fully balanced instability mode as Ro, Fr $\rightarrow 0$. Nevertheless, in spite of the great changes in spatial scale and growth rate induced during frontogenesis for both the 2D frontal flow and the 3D fluctuation fields (with more modest changes in their (X, Z) spatial pat-

terns), there is a nearly geostrophic, baroclinic-instability-like, 3D fluctuation growth mode whose growth and shape are robustly persistent during frontogenesis. As an approximate summary, we can say that the changes of scale and growth rate in the 3D instability with increasing t_0 simply track the sharpening front and increasing 2D shear.

As stated above, the maximum 3D fluctuation growth rate, $\sigma_{\max}$, approximately keeps pace with the quasi-exponentially increasing $\widetilde{\mathrm{Ro}}$ and $\widetilde{\mathrm{Fr}}$ values during frontogenesis (Fig. 2). This suggests that the frontal instability rate is primarily determined by the frontal shear magnitude, rather than the frontogenetic deformation rate itself. This is tested by a sequence of cases with
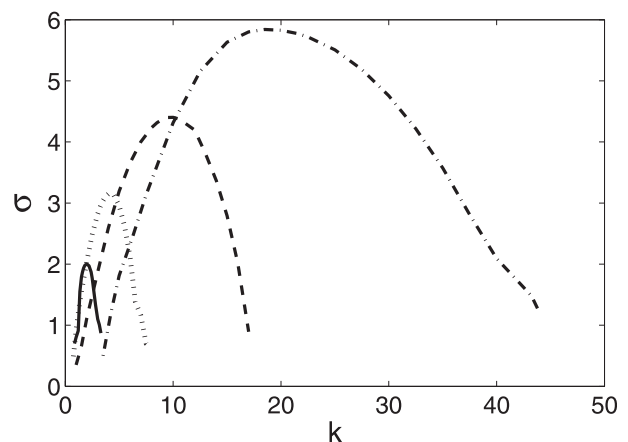

FIG. 9. The 3D fluctuation growth rate $\sigma(k)$ for $\alpha_0 = 1.0$ for a k range in which σ is large enough to be well determined by breeding and the modal shape is similar to the shape at the maximum growth wavenumber $k_{\max}$: $t_0 = 0.0$, solid; $t_0 = 0.5$, dotted; $t_0 = 1.0$, dashed; and $t_0 = 1.5$, dotted–dashed. For comparison, successive $e^{\beta(t_0)}$ values are 1.0, 1.45, 2.40, and 3.96.

TABLE 1. Normalized 3D fluctuation energy fraction and conversion rates with the standard initial profile (10) and $\alpha_0 = 1.0$ for the fastest growing modes. The normalization is by total energy.

t_0	$e^{\beta(t_0)}$	$k_{\max}$	$\sigma_{\max}$	$\mathcal{K}$	$\mathcal{DF}$	$\mathcal{PK}$	$\mathcal{RF}$	$\mathcal{BF}$
0.0	1.00	2.0	2.00	0.42	0.00	0.36	1.32	2.69
0.5	1.45	4.0	3.17	0.46	0.22	1.09	1.57	4.58
1.0	2.40	9.5	4.39	0.45	0.13	1.79	2.09	6.65
1.5	3.96	18.5	5.95	0.47	−0.04	2.51	3.13	9.07

different values of α_0. In each case, $\widetilde{\mathrm{Ro}}$, $\widetilde{\mathrm{Fr}}$, and $\sigma_{\max}$ grow quasi-exponentially in time, with exponents approximately proportional to $\beta \sim \alpha_0 t_0$. Thus, with increasing α_0, $\sigma_{\max}(t)$ is a much steeper function of t since a given 2D frontal strength occurs at increasingly earlier t_0. To factor out this effect, we compare different α_0 cases by picking comparison times t_0 that have similar values of $\widetilde{\mathrm{Ro}}$ and $\widetilde{\mathrm{Fr}}$ (Table 2 is based on a survey with finite resolution in t_0 and k). The result is that $(k_{\max}, \sigma_{\max})$ are only weakly increasing functions of α_0, although their enhancement increases somewhat for larger α_0. [In practice we are limited by our experimental protocol (section 3) from looking at very large values of α_0 since the comparable t_0 value drops well below the spinup interval Δt for $\alpha(t)$.] A visual comparison of the 3D modal patterns for these different cases with those in Fig. 7 shows that they differ only moderately with α_0. This result, that even the normalized frontal instability rate increases with the deformation rate, is contrary to Bishop (1993). This discrepancy is discussed in section 9.

6. Fluctuation frontolysis and restratification

Section 5 shows that 3D fluctuations extract energy mostly from the 2D frontal flow, increasingly with t_0. This indicates that fluctuations play some role in retarding frontogenesis (often referred to as frontolysis) at least in an integral sense. Here we refine that characterization by examining the frontogenetic tendency balance (Giordani and Caniaux 2001) derived from the alongfront-averaged buoyancy conservation equation including the nonlinear eddy flux. For simplicity we write it in untransformed coordinates (also used in the appendix for the energy balance), even though in practice we evaluate its component terms from our solution in transformed coordinates:

$$\frac{\partial}{\partial t}\left[\frac{1}{2}(\partial_x b)^2\right] = -(\partial_x b)\partial_x[\partial_x(ub) + \partial_z(wb')]$$

$$- \frac{\partial_x b}{2}\partial_x[\partial_x(\hat{u}:\hat{b}) + \partial_z(\hat{w}:\hat{b})],$$

$$\equiv \mathcal{T}_{2D} + \mathcal{T}_F. \qquad (11)$$

The eddy-flux symbol $\hat{c}:\hat{d}$ is defined as $\mathrm{Re}[\hat{c}]\,\mathrm{Re}[\hat{d}] + \mathrm{Im}[\hat{c}]\,\mathrm{Im}[\hat{d}]$. The final line collects the frontogenetic

tendencies in the preceding right-side line into advection by the 2D circulation $\mathcal{T}_{2D}$ and eddy fluxes $\mathcal{T}_F$.

In Fig. 11 the pattern of the advective effect of the secondary circulation $\mathcal{T}_{2D}$ is familiar from previous studies of frontogenesis. It has a dipole structure, mainly due to lateral advection, indicating displacement of the frontal center toward the dense side. Since the positive lobe is stronger than the trailing negative lobe, it implies a frontogenetic growth of frontal strength on the dense side. On the other hand, the eddy-flux effect $\mathcal{T}_F$ is overwhelmingly negative (i.e., frontolytic): $\mathcal{T}_F$ is nearly centered on the peak frontal strength (Fig. 4) and it somewhat trails the position of the peak frontogenesis in $\mathcal{T}_{2D}$. This suggests that fluctuation frontolysis will retard frontogenesis but might not entirely stop it since the peaks of $\mathcal{T}_F$ and $\mathcal{T}_{2D}$ are not exactly coincident. Nevertheless, fluctuation frontolysis may play a significant role in reducing the 2D frontogenesis induced by the deformation flow, changing the shape of the evolving frontal flow at the least, but potentially providing a mechanism for frontal arrest at a finite scale. We leave further investigation of finite-amplitude fluctuation effects in modifying frontogenesis to the future.

Another diagnostic measure of fluctuation effects on the front is the eddy-induced circulation that provides a mean Lagrangian transport of buoyancy and other material tracers (Gent and McWilliams 1990). The eddy-induced overturning streamfunction in the cross-front plane is defined by

$$\psi_* \equiv \frac{1}{2(\nabla b)^2}[(\hat{w}:\hat{b})\partial_x b - (\hat{u}:\hat{b})\partial_z b], \qquad (12)$$

with associated "bolus" velocities $u_* = \partial_z \psi_*$ and $w_* = -\partial_x \psi_*$ [Ferrari et al. (2008), but note the opposite sign convention here].

The overturning streamfunction ψ_* for our standard frontogenetic case ($\alpha_0 = t_0 = 1.0$, $k = 9.5$) is shown in Fig. 12. It is one signed (positive) in ψ_*, implying a counterclockwise circulation centered on the instantaneous frontal center. Its sense of circulation therefore generally reinforces the 2D secondary circulation ψ in the lower part of the front (Fig. 5).[4] The most significant

---

[4] In the major midlatitude, climatologically forced jets (e.g., the jet stream, Antarctic Circumpolar Current), the eddies are generated primarily by baroclinic instability, as here; the mean secondary circulations (Ferrell and Deacon cells, respectively) have rising motion on the dense side, the opposite direction as here; and the eddy-induced circulations are in the same direction as here. Thus, the mean and eddy-induced secondary circulations tend to cancel each other in turbulent-equilibrium jets, while they are reinforcing during unstable frontogenesis in a deformation flow.
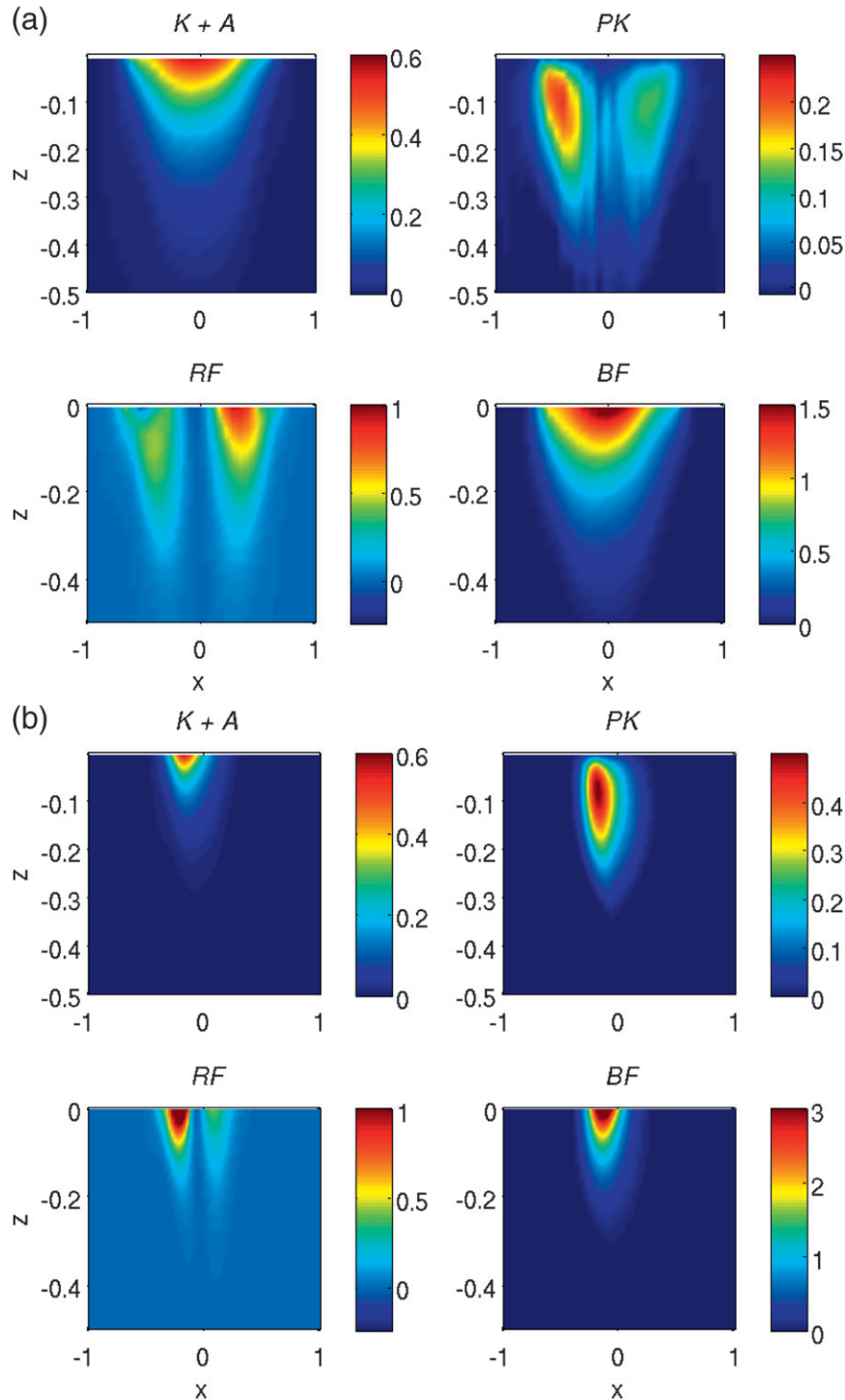
FIG. 10. Fluctuation energy and energy-conversion integrands for the fastest growing modes at (top) $t_0 = 0.0$ (with $k = 2$) and (bottom) $t_0 = 1.0$ (with $k = 9.5$) with $\alpha_0 = 1.0$: (top left) the total energy $\mathcal{K} + \mathcal{A}$ (with the mode normalized such that $\max_{x,z}|\hat{b}| = 1.0$) and conversions divided by the integrated total energy (i.e., energy change rates); (top right) $\mathcal{PK}$, (bottom left) $\mathcal{RF}$, and (bottom right) $\mathcal{BF}$.

TABLE 2. Fastest growing 3D fluctuation modes for different values of the asymptotic deformation rate α_0. The t_0 values are chosen for approximate equivalence of the $\widetilde{\mathrm{Ro}}(t_0)$ and $\widetilde{\mathrm{Fr}}(t_0)$ values with the standard case ($\alpha_0 = t_0 = 1.0$).

α_0	t_0	$\widetilde{\mathrm{Ro}}$	$\widetilde{\mathrm{Fr}}$	k_{max}	σ_{max}
0.33	2.8	0.56	0.76	9.5	4.1
1.0	1.0	0.55	0.75	9.5	4.4
3.0	0.42	0.56	0.76	9.9	5.7
10.0	0.21	0.58	0.73	11.1	9.5

structural difference is that ψ_* does not have an interior maximum whereas ψ does. In general, ψ_* defines an incompressible circulation that must satisfy the surface boundary condition of $\psi_* = 0$ at $z = 0$. However, in the problem we have posed—with an essentially inviscid flow and significant stratification extending up to the top surface (hence, neither $(\hat{u} : \hat{b})$ nor $\partial_z b$ decrease toward the surface)—the leftward return-flow branch, where ψ_* decreases toward zero at the top boundary, is singularly compressed into the topmost grid cell (and not plotted in Fig. 12). In the ocean and in oceanic general circulation models that include ψ_* as a parameterization for eddy flux, the surface return flow primarily occurs within the turbulent boundary layer where $\partial_z b \approx 0$, as sketched in Fig. 4 of Ferrari et al. (2008) for an unstable stationary frontal flow. The proper interpretation of ψ_* in this solution is that the 3D fluctuations contribute to buoyancy restratification and potential-to-kinetic energy conversion (as expected for a baroclinic instability), reinforcing these same effects in 2D frontogenesis, but unlike ψ they do not advectively contribute to frontogenesis within the

interior. Further consideration of the implied return-flow branch in ψ_* is deferred to cases with a weakly stratified surface layer (section 8) where it is explicitly manifest.

7. Transient fluctuation growth

In the breeding approximation (section 3), we determine the fastest-growing 3D modes for each wavenumber k while effectively freezing the 2D frontogenesis at a particular time t_0. This is justified by the approximation $\sigma \gg \alpha$ that is confirmed a posteriori (section 5). Now, however, we relax the approximation and examine the simultaneous 2D and 3D evolution, using the fastest-growing mode and its associated k value as the 3D initial condition at $t = t_0$. In Fig. 13, we show the results of three different t_0 values, each integrated forward to the final time of $t = 1.5$. In each case the 3D amplitude grows exponentially at the expected growth rate σ (Table 1) for an early interval, but later the growth curve falls below a simple exponential form, although significant growth continues to occur. For the $t_0 = 1.0$ case, the exponential growth does not appreciably abate over the time of integration. The evolving 3D fluctuation patterns (not shown) continue to show the familiar scale contractions in (x, z) (e.g., as in Fig. 7) following along with the 2D frontogenesis. This continuing transient growth occurs in spite of substantial changes in the 2D frontal shape and the k value and associated 3D fluctuation pattern with maximum growth rate at t_0. It is also consistent with the growing k bandwidth of unstable modes as t_0 increases (Fig. 9); for example, the transient
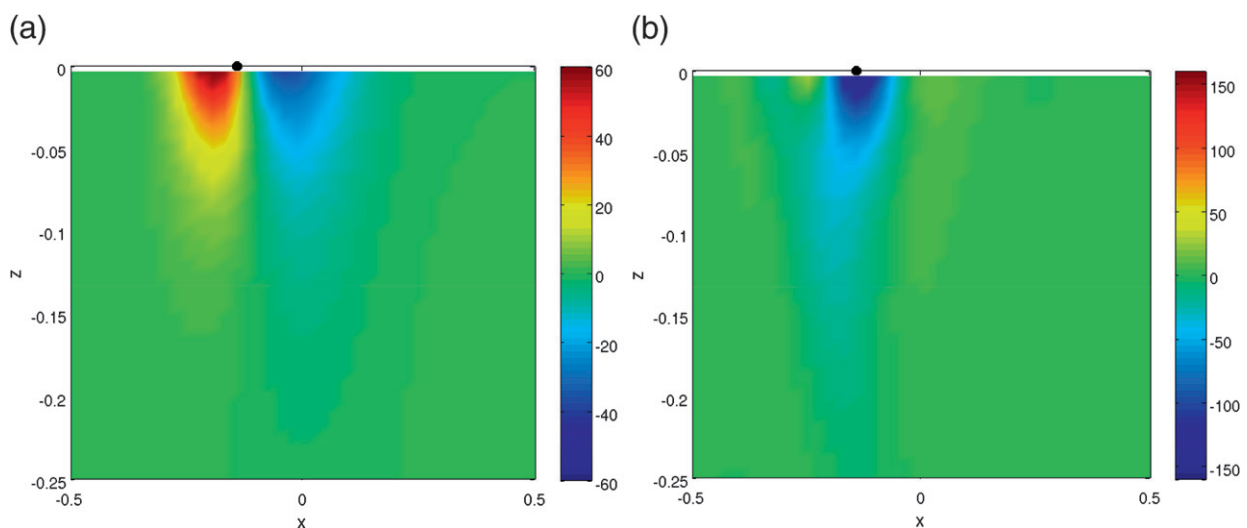

FIG. 11. Frontogenetic tendencies in (11) for the standard initial profile (10) at $t_0 = 1.0$ with $\alpha_0 = 1.0$ and the fastest growing mode (Table 1): (left) $\mathcal{T}_{2D}(x, z)$ and (right) $\mathcal{T}_F(x, z)$. In $\mathcal{T}_F$ the fluctuation mode is normalized such that $\max_{x,z}|\hat{b}| = 1.0$; dots on the x axes denote the position of maximum 2D frontal strength $(\partial_x b)^2/2$ (Fig. 4, right panel).
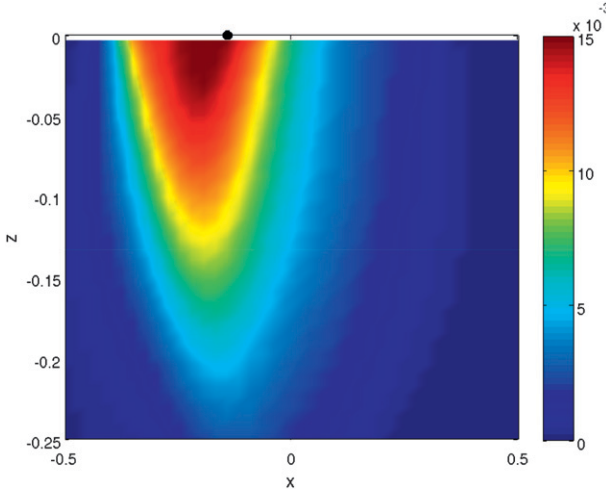
FIG. 12. Eddy-induced streamfunction ψ_* in (12) for the fastest growing mode (Table 1) at $t_0 = 1.0$ with $\alpha_0 = 1.0$ and $k = 9.5$. The fluctuation mode is normalized such that $\max_{x,z}|\hat{b}| = 1.0$; the dot on the x axis denotes the center of the 2D front at this time (Fig. 4, right panel).
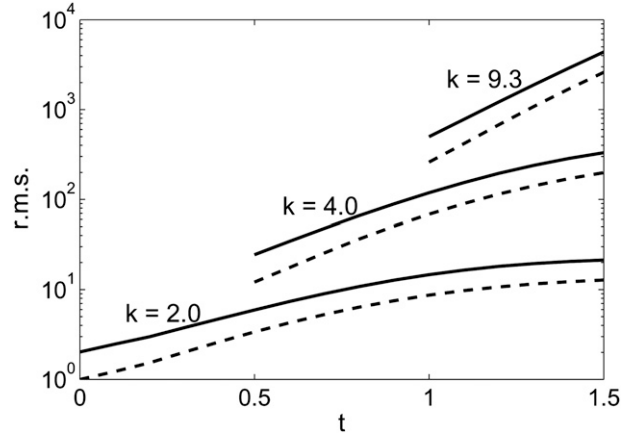

FIG. 13. Growth of rms 3D fluctuation amplitudes (cf. Fig. 6) for $\hat{v}$ (dashed) and $\hat{b}$ (solid) in three cases with $\alpha_0 = 1.0$ and the simultaneous evolution of the 2D front and 3D fluctuations. The 2D evolution is continuous from $t = 0.0$. For each case at the alternative starting times of $t_0 = 0.0, 0.5$, and 1.0 the 3D initial condition is the fastest growing mode determined by breeding with the indicated k value. The 3D modes have arbitrary initial amplitudes chosen for graphical clarity.

growth initiated at $t_0 = 0.5$ with $k = 4.0$ exhibits growth at $t = 1$ with a rate very close to the bred mode at $t_0 = 1$ with $k = 4.0$. Thus, the reliability of the breeding approximation is further confirmed. More importantly, the transient evolutions show widespread and efficient fluctuation growth during active frontogenesis, even among nonexponentially growing 3D fluctuation patterns. In combination with the rather broad $\sigma(k)$ curves with overlap in their k ranges at different t_0 (Fig. 9), we can expect broadband fluctuation growth as frontogenesis proceeds, where the emergent 3D fluctuation patterns will be influenced by the extant perturbations in particular realizations.

8. Profile sensitivities

As remarked in section 3, geostrophic shear instability is notoriously sensitive to details of the mean-flow profile. We will not make a comprehensive survey for the present problem. Nevertheless, we briefly describe the results for some alternative initial frontal profiles to give a sense of the typicality of the behavior presented in sections 4–6.

a. Wider front

We broaden the initial frontal flow by choosing a smaller B value in (10), namely, $B = 1.0$. This makes the initial $\widetilde{Ro}$ value smaller, while keeping $\widetilde{Fr}(0)$ the same. During frontogenesis both $\widetilde{Ro}(t)$ and $\widetilde{Fr}(t)$ grow similar to the standard case (Fig. 2). The 3D instability mode at $t_0 = 0.0$ (i.e., with $\alpha = 0.0$) occurs at a somewhat smaller peak-growth k value of 1.4 (cf. 2.0 with the standard

profile) and has a weaker growth rate of $\sigma = 1.3$ (cf. 2.0). This is more purely a baroclinic instability mode than the standard case, and the associated $\mathcal{RF}$ is even weakly negative in an integral sense, implying countergradient fluctuation horizontal momentum flux (as in the jet stream and Antarctic Circumpolar Current), especially on the dense, cyclonic-shear side of the front (n.b., for the standard case in Fig. 10, this is the side of the front where $\mathcal{RF}$ is least positive at $t_0 = 0.0$). Consequently, $\mathcal{PK}$ is larger in this case. By $t_0 = 1.0$, however, the differences between this case and the standard one in the various 2D and 3D measures mostly persist in their sense but diminish in magnitude. The peak growth $\sigma = 4.6$ at $k = 6.0$ (cf. 4.4 at 9.5) is slightly larger here.

b. Narrower, deeper front

We sharpen and deepen the initial frontal flow by choosing a larger B and smaller A value in (10), namely, $B = 3.0$ and $A = 2.0$. This implies a larger $\widetilde{Ro}(0)$ and smaller $\widetilde{Fr}(0)$ compared to the standard case (Fig. 2). Yet, again there is nearly exponential growth $\sim e^\beta$ in both $\widetilde{Ro}(t)$ and $\widetilde{Fr}(t)$. The peak-growth 3D mode at $t_0 = 0.0$ has larger $\sigma = 2.9$ at larger $k = 2.6$ (cf. 2.0 at 2.0), and the associated $\mathcal{RF}$ is positive and much larger than $\mathcal{BF}$, while $\mathcal{PK} < 0$. Therefore, this case is primarily a barotropic instability rather than a baroclinic one. Barth (1994) similarly finds that the dominant fluctuation energy source for a stationary 2D frontal flow could shift between $\mathcal{BF}$ and $\mathcal{RF}$ as the dominant shear shifts between horizontal and vertical. At $t_0 = 1.0$ the peak growth σ is 3.9 at $k = 12.8$ (cf. 4.4 at 9.5), but both $\mathcal{RF} \gg \mathcal{BF}$
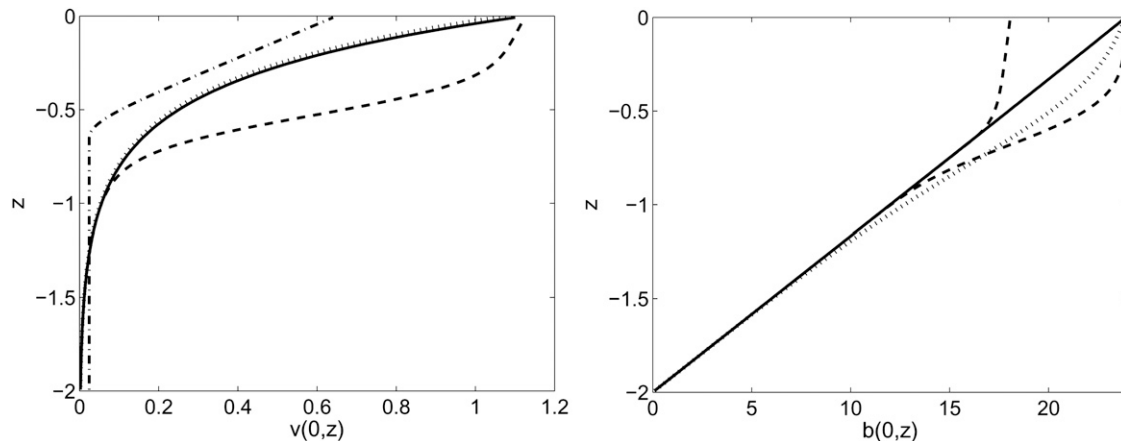
FIG. 14. Initial vertical profiles at the center of the front at $t = 0.0$: (left) $v(0, z)$ and (right) $b(0, z)$. The standard case (10) is the solid curve, and the alternative mixed layer cases are denoted by M1 (dashed), M2 (dotted), and M3 (dotted–dashed). The v profiles are as in the standard and M2 cases.

and $\mathcal{PK} < 0$ still hold, albeit to a lessening relative degree with increasing t_0. This and the preceding profile sensitivities confirm that the frontal instability mechanism is mixed baroclinic–barotropic in type. It is also consistent with the frontal instability behavior—with $\widetilde{Ro} > \widetilde{Fr}$ and fluctuation generation dominated by the $\mathcal{RF} > 0$—in the simulations by Molemaker et al. (2009), where sometimes the instability is so effective that frontogenesis is arrested.

c. Mixed layer fronts

Because of surface fluxes and boundary layer turbulence, the stratification usually weakens in the upper ocean. We do not include the surface fluxes and enhanced turbulent mixing explicitly in our problem, but we can partially investigate their effects with modified initial profiles in $v(x, z)$ and $b(x, z)$. We consider three alternative profiles to (10): M1 uses a vertical stretching function applied to both $v(x, z)$ (hence $b'(x, z)$) and $\langle b \rangle(z)$ that diminishes the vertical gradients within a specified distance from the surface while preserving the maximum value of v at the surface and the profiles at depth, M2 applies this stretching function only to $\langle b \rangle$ and leaves v and b' unaltered from (10), and M3 imposes a linear shear in $v(0, z)$ and reduced stratification in $\langle b \rangle$ over a vertical distance similar to the M1 and M2 cases in a way that spatially separates the near-surface shear layer from the quiescent stratified interior [n.b., this is essentially the structure of the "mixed layer instability" profile in Boccaletti et al. (2007)]. Rather than express these modifications in formulas, we show them graphically (Fig. 14). In all cases the horizontal frontal structure is kept the same as in (10) with the same value of $B = 2.0$.

Case M1 has initial values of $\widetilde{Ro}$ and $\widetilde{Fr}$ similar to the standard case, but these nondimensional numbers do not grow appreciably during frontogenesis since the largest

$|\partial_x b|$ occurs within the stratified interior rather than at the surface where frontogenesis can be most effective due to the constraint of zero vertical velocity, hence large vertical divergence (Lapeyre et al. 2006). The peak-growth instability is a mixed barotropic–baroclinic type with $\sigma = 3.2$ at $k = 2.0$ at $t_0 = 0.0$ (cf. 2.0 at 2.0) and $\sigma = 5.1$ at $k = 19.0$ at $t_0 = 1.0$ (cf. 4.4 at 9.5). Thus, 3D fluctuation growth is comparably strong and increases even more under the action of a deformation flow when the frontogenesis shifts to being subsurface, although the 2D frontal structure and 3D mode patterns are quite different (not shown).

Case M2 has the same initial surface $\partial_x b$ and $\partial_z v$ as the standard case, albeit with reduced near-surface stratification. Consequently, its $\widetilde{Ro}(t)$ and $\widetilde{Fr}(t)$ show the same kind of frontogenetic growth as in Fig. 2. The $t_0 = 0.0$ 3D instability mode also has a similar $\sigma = 2.2$ at $k = 2.0$ (cf. 2.0 at 2.0) with $\mathcal{BF} > \mathcal{RF} > 0$ and $\mathcal{PK} > 0$. Under frontogenesis, however, the growth in peak-growth k and σ values is much greater with the reduced stratification; for example, at $t_0 = 1.0$, $\sigma = 8.2$ at $k = 14.0$ (cf. 4.4 at 9.5). Also, $\mathcal{RF}$ becomes negative at late t_0 (as in the wider front case, mainly on the heavy, cyclonic-shear side of the front), indicating an even greater degree of dominance by baroclinic fluctuation energy generation for this frontal profile. The modal structure is illustrated in Fig. 15. The shape of $\hat{b}$ is similar to the standard case (Fig. 7) except that it extends somewhat more deeply through the weakly stratified surface layer, and ψ_* is again a single positive cell, as in Fig. 12, except that it also reaches more deeply and nearly closes its surface return circulation within the interior (i.e., $\psi_* \to 0$ as $z \to 0$) since $\partial_z b$ becomes small in (12). This confirms the comment in section 6 that a weakly stratified surface layer allows the ψ_* circulation to be closed within the resolved domain. Also, the mode-normalized, eddy-induced
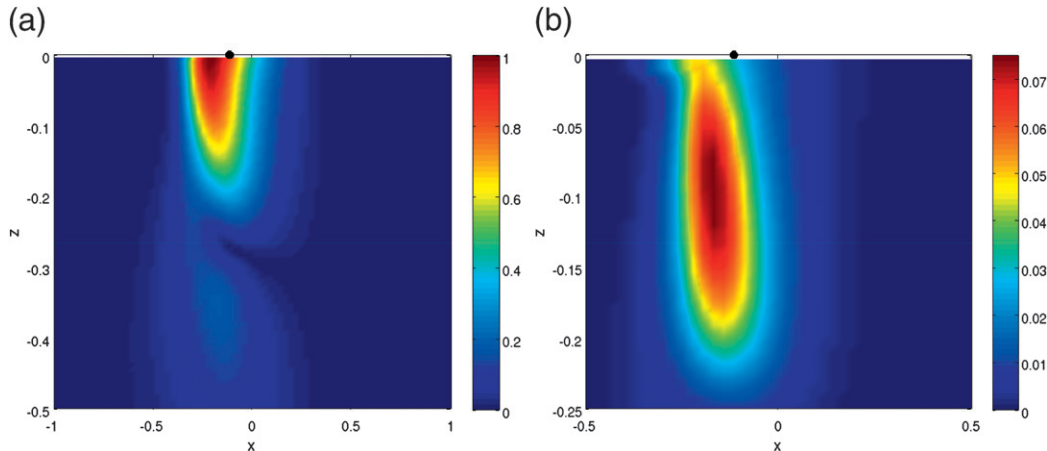
FIG. 15. Fastest growing 3D fluctuation for the mixed layer profile M2 with $\alpha_0 = 1.0$ at $t_0 = 1.0$ with $\sigma_{max} = 8.2$ and $k_{max} = 14.0$: (left) magnitude of the complex buoyancy field $|\hat{b}|$ and (right) eddy-induced streamfunction ψ_* in (12). The fluctuation mode is normalized such that $\max_{x,z} |\hat{b}| = 1.0$. The dot on the x axis again denotes the position of maximum frontal strength. Note the different subdomains in these two plots and the change of color scale for ψ_* compared to Fig. 12.

circulation is stronger because the reduced mixed layer stratification reduces the denominator in (12).

Case M3 is distinctly different from all other cases because its initial instability scale is much smaller and its growth rate is larger: at $t_0 = 0.0$, $\sigma = 5.2$ at $k = 7.0$ (cf. 2.0 at 2.0). This is also a rather pure form of baroclinic instability with $\mathcal{RF} < 0$ (though small in magnitude compared to $\mathcal{BF}$) and $\mathcal{PK} > 0$. These properties are consistent with the stationary-flow instability results in Boccaletti et al. (2007). With $\alpha \neq 0$, the 2D frontogenesis behavior for M3 is similar to the standard profile, as are the relative changes of a decreasing alongfront scale and an increasing growth rate with increasing t_0 for the 3D fluctuation modes [e.g., at $t_0 = 1.0$, $\sigma = 8.6$ at $k = 14.0$ (cf. 4.4 at 9.5)].

In all three mixed layer cases the growth rates are increased, both initially and during frontogenesis, due to reduced stratification N. This is expected since the dimensional scaling of σ with Vf/Nh is a classical property of baroclinic instability (Eady 1949).

In summary, this fragmentary survey of profile sensitivities indicates that increasing σ, shifting to larger k, and increasing the dominance of $\mathcal{BF}$ are all robust 3D fluctuation behaviors under the action of a deformation flow and the associated 2D frontogenesis, even though the quantitative details vary from case to case.

9. Discussion

Near-surface 2D frontogenesis induced by a deformation flow enhances the growth of 3D fluctuations that occur on an ever smaller scale and with an ever larger growth rate as the 2D front progressively sharpens. This behavior is consistent with previous instability studies of

stationary flows in its dependences on the scale and shear magnitude (or Ro and Fr value) of the background flow. The 3D fluctuation growth further increases with a larger deformation rate. The fluctuations grow by a combination of baroclinic and barotropic energy conversions from the frontal flow, with the former dominating for most of the situations that we have examined. The alongfront-averaged buoyancy fluxes of the growing fluctuations resist the 2D frontogenesis through a frontolytic tendency in $(\partial_x b)^2$ and they also augment the buoyancy restratification and potential-to-kinetic energy conversion tendencies of the 2D frontogenesis itself. The eddy-induced cross-frontal overturning streamfunction ψ_* is also indicative of isopycnal flattening and restratification by the 3D fluctuations. These behaviors are remarkably robust across a range of initial horizontal and vertical shear and stratification profiles. In the ranges surveyed here, all of the 3D instability examples are essentially of a single type, morphing from a primarily baroclinic energy source to a barotropic one as the ratio of 2D shear to horizontal shear decreases, consistent with previous instability studies of stationary frontal flows. Our primary conclusion, therefore, is that active deformation in frontogenesis does not greatly alter the instability mechanism.

This conclusion is starkly in contrast to traditional frontogenesis models with uniform potential vorticity where either such 3D frontal-shear instabilities do not occur [with only one vertical boundary (Held et al. 1995)] or where deformation acts to suppress the instability [with two vertical boundaries (Bishop (1993)]. The conclusion also differs from the fully barotropic regime where a deformation flow can stabilize a sharpening, otherwise unstable, horizontal shear layer. These differences imply that

the nature of the instability in a deformation flow for each of these three regimes (i.e., mixed baroclinic–barotropic instability with interior potential vorticity gradients, baroclinic instability due to surface buoyancy gradients in the Eady model, and barotropic instability of a vorticity filament) is importantly different in its behavior. However, the same kinds of instability differences also occur for stationary flows in these three regimes in a way characterized by their different contributions to the Rayleigh/Charney–Stern conditions.

Our results are mostly consistent with those of Spall (1997), whose flow configuration is qualitatively similar to ours. Here we have explored 3D fluctuation growth with larger values of Ro, Fr, and α, albeit with a linearized dynamical approximation. However, since we find an increasing growth rate with all these parameters, we disagree with his interpretation that a larger deformation rate stabilizes the flow by the mechanism presented in Bishop (1993); rather, it seems more likely that large α, narrow-front instabilities are suppressed by his choices for too large an eddy viscosity value and/or too coarse a grid resolution to resolve the small instability scales. (This speculation could only be confirmed by extending his study.) Thus, strong frontal instability is most likely to occur in the submesoscale regime in the ocean.

Frontogenesis and frontal instability, and the associated material transport and turbulent cascade of variance toward small-scale mixing, are evidently important dynamical processes in the submesoscale regime in the upper ocean (and likely the lower atmosphere as well). The present study demonstrates a significant linear instability for Rossby and Froude numbers ranging from small to $\mathcal{O}(1)$ values. This result naturally points toward further studies of finite-amplitude 3D frontal dynamics, later-stage frontogenetic instabilities for larger Ro and Fr values, and nonconservative influences by surface fluxes and boundary layer turbulence. We have also seen, but largely avoided in this paper by the problem selection, that spontaneous inertia–gravity wave emission during frontogenesis is occasionally quite efficient in both 2D and 3D, for example, in association with rapidly changing deformation flows. It remains an open question as to what type of instability or turbulence ultimately limits frontogenesis and frontal "collapse" under conditions of persistent deformation (Hoskins 2003), but the instability mode presented here, with its attendant frontolytic effects, is one candidate.

APPENDIX

Fluctuation Energy and Conversion Rates

The linear fluctuation equations (9) can be manipulated into energy balances. We first form a balance equation for the fluctuation kinetic energy density,

$$\mathcal{K} = \frac{1}{2}(\varepsilon^2|\hat{u}|^2 + |\hat{v}|^2 + \varepsilon^2\lambda^2|\hat{w}|^2), \qquad \text{(A1)}$$

by multiplying the momentum equations by the complex conjugate fields $\hat{u}^\dagger$, $\hat{v}^\dagger$, and $\hat{w}^\dagger$, respectively; summing them and adding the total to its complex conjugate; and dividing by 2Ro. This yields

$$\frac{d}{dt}\int\int \mathcal{K}\, dx\, dz = \mathcal{DF} + \mathcal{RF} + \mathcal{PK}. \qquad \text{(A2)}$$

The right-side conversion terms are the fluctuation energy generation from the deformation flow,

$$\mathcal{DF} = \alpha(t)\int\int (\varepsilon^2|\hat{u}|^2 - |\hat{v}|^2)\, dx\, dz;$$

the generation from the 2D frontal flow through fluctuation Reynolds stress,

$$\mathcal{RF} = -\int\int (\varepsilon^2(\hat{u}:\hat{u}\partial_x u + \hat{u}:\hat{w}\partial_z u) + (\hat{v}:\hat{v}\partial_x v + \hat{v}:\hat{w}\partial_z v)$$
$$+ \varepsilon^2\lambda^2(\hat{u}:\hat{w}\partial_x w + \hat{w}:\hat{w}\partial_z w))\, dx\, dz; \qquad \text{(A3)}$$

and the conversion from fluctuation potential energy,

$$\mathcal{PK} = \frac{1}{\text{Ro}}\int\int (\hat{w}:\hat{b})\, dx\, dz.$$

For complex fields $\hat{c}$ and $\hat{d}$, we define $\hat{c}:\hat{d} = \text{Re}[\hat{c}]\,\text{Re}[\hat{d}] + \text{Im}[\hat{c}]\,\text{Im}[\hat{d}]$; hence, $\hat{c}:\hat{c} = |\hat{c}|^2$.

A companion available potential energy balance can be derived for

$$\mathcal{A} = \frac{1}{2\mathcal{N}^2}|\hat{b}|^2,$$

with

$$\mathcal{N}^2(z) = \frac{\text{Ro}^2}{\text{Fr}^2}\partial_z\langle b\rangle.$$

It is derived from the fluctuation buoyancy equation similar to the kinetic energy derivation procedure and has the form:

$$\frac{d}{dt} \iint \mathcal{A}\, dx\, dz = \mathcal{BF} - \mathcal{PK}, \qquad \text{(A4)}$$

where the fluctuation energy generation from the 2D frontal flow through fluctuation buoyancy flux and variance is

$$\mathcal{BF} = -\iint \frac{1}{\mathcal{N}^2}\left(\hat{u} : \hat{b}\, \partial_x b + \hat{w} : \hat{b}\left(\partial_z b - \frac{\mathcal{N}^2}{\mathrm{Ro}} \right) + \frac{\hat{b} : \hat{b}}{2}\, w\, \frac{\partial_{zz}\langle b \rangle}{\partial_z \langle b \rangle} \right) dx\, dz.$$

In deriving this balance we have assumed that $\langle b \rangle(z)$ is independent of time and $\partial_z \langle b \rangle > 0$ everywhere.

By combining these equations we obtain the total fluctuation energy balance:

$$\frac{d}{dt} \iint (\mathcal{K} + \mathcal{A})\, dx\, dz = \mathcal{DF} + \mathcal{RF} + \mathcal{BF}. \qquad \text{(A5)}$$

In Fig. 10 and Table 1, the quantities in this balance equation are normalized by the integrated fluctuation energy, $\iint (\mathcal{K} + \mathcal{A})\, dx\, dz$. The sum of the conversions on the rhs of (A5) after this normalization is equal to 2σ since the fluctuation energy is a quadratic functional of the fluctuation field amplitudes (n.b., Table 1 within the discretization error). Analogous relations exist in the (X, Y, Z) coordinates, with $dx\, dy\, dz = e^{-\beta_z}\, dX\, dY\, dZ$, $\partial_x = e^{\beta}\partial_X$, and $\partial_z = e^{\beta_z}\partial_Z$.

REFERENCES

Barth, J. A., 1994: Short-wavelength instabilities on coastal jets and fronts. *J. Geophys. Res.,* **99,** 16 095–16 115.

Bergeron, T., 1928: Uber die dreidimensional verknupfende wetteranalyse I. *Geofys Publ.,* **5,** 1–111.

Bishop, C. H., 1993: On the behavior of baroclinic waves undergoing horizontal deformation. II. Error-bound amplification and Rossby wave diagnostics. *Quart. J. Roy. Meteor. Soc.,* **119,** 241–267.

Bjerknes, J., 1919: On the structure of moving cyclones. *Geofys. Publ.,* **1,** 95–99.

Boccaletti, G., R. Ferrari, and B. Fox-Kemper, 2007: Mixed layer instabilities and restratification. *J. Phys. Oceanogr.,* **37,** 2228–2250.

Capet, X., J. C. McWilliams, M. J. Molemaker, and A. Shchepetkin, 2008: Mesoscale to submesoscale transition in the California Current System: Frontal processes. *J. Phys. Oceanogr.,* **38,** 44–64.

Castelao, R., T. Mavor, J. Barth, and L. Breaker, 2006: Sea surface temperature fronts in the California Current System from geostationary satellite observations. *J. Geophys. Res.,* **111,** C09026, doi:10.1029/2006JC003541.

Dritschel, D. G., P. H. Haynes, M. N. Jukes, and T. G. Shepherd, 1991: The stability of a two-dimensional vorticity filament under uniform strain. *J. Fluid Mech.,* **230,** 647–665.

Eady, E. T., 1949: Long waves and cyclone waves. *Tellus,* **1,** 33–52.

Eliassen, A., 1984: The Charney–Stern theorem on barotropic–baroclinic instability. *Pure Appl. Geophys.,* **121,** 563–572.

Ferrari, R., J. C. McWilliams, V. M. Canuto, and M. Dubovikov, 2008: Parameterization of eddy fluxes near oceanic boundaries. *J. Climate,* **21,** 2770–2789.

Flament, P., L. Armi, and L. Washburn, 1985: The evolving structure of an upwelling filament. *J. Geophys. Res.,* **90,** 11 765–11 778.

Gent, P. R., and J. C. McWilliams, 1990: Isopycnal mixing in ocean circulation models. *J. Phys. Oceanogr.,* **20,** 150–155.

Giordani, H., and G. Caniaux, 2001: Sensitivity of cyclogenesis to sea surface temperature in the northwestern Atlantic. *Mon. Wea. Rev.,* **129,** 1273–1295.

Heifetz, E., C. H. Bishop, B. J. Hoskins, and J. Methven, 2004: The counter-propagating Rossby-wave perspective on baroclinic instability. I: Mathematical basis. *Quart. J. Roy. Meteor. Soc.,* **130,** 211–231.

Held, I., R. Pierrehumbert, S. Garner, and K. Swanson, 1995: Surface quasi-geostrophic dynamics. *J. Fluid Mech.,* **282,** 1–20.

Hoskins, B. J., 1974: The role of potential vorticity in symmetric stability and instability. *Quart. J. Roy. Meteor. Soc.,* **100,** 480–482.

——, 1982: The mathematical theory of frontogenesis. *Annu. Rev. Fluid Mech.,* **1,** 131–151.

——, 2003: Back to frontogenesis. *A Half Century of Progress in Meteorology: A Tribute to Richard Reed, Meteor. Monogr.,* No. 53, Amer. Meteor. Soc., 49–59.

——, and F. P. Bretherton, 1972: Atmospheric frontogenesis models: Mathematical formulation and solution. *J. Atmos. Sci.,* **29,** 11–37.

Klemp, J. B., and D. R. Duran, 1983: An upper boundary condition permitting internal gravity wave radiation in numerical mesoscale models. *Mon. Wea. Rev.,* **111,** 430–444.

Lapeyre, G., P. Klein, and B. L. Hua, 2006: Oceanic restratification forced by surface frontogenesis. *J. Phys. Oceanogr.,* **36,** 1577–1590.

McWilliams, J. C., 2006: *Fundamentals of Geophysical Fluid Dynamics.* Cambridge University Press, 249 pp.

Molemaker, M. J., and H. A. Dijkstra, 2000: Stability of a cold-core eddy in the presence of convection: Hydrostatic versus nonhydrostatic modeling. *J. Phys. Oceanogr.,* **30,** 475–494.

——, J. C. McWilliams, and X. Capet, 2009: Balanced and unbalanced routes to dissipation in an equilibrated Eady flow. *J. Fluid Mech.,* in press.

Schär, C., and H. C. Davies, 1990: An instability of a mature cold front. *J. Atmos. Sci.,* **47,** 929–950.

Snyder, C., W. C. Skamarock, and R. Rotunno, 1993: Frontal dynamics near and following frontal collapse. *J. Atmos. Sci.,* **50,** 3194–3211.

Song, Y., and N. Nakamura, 2000: Eady instability of isolated baroclinic jets with meridionally varying tropopause height. *J. Atmos. Sci.,* **57,** 46–65.

Spall, M. A., 1997: Baroclinic jets in confluent flow. *J. Phys. Oceanogr.,* **27,** 1054–1071.

Toth, Z., and E. Kalnay, 1997: Ensemble forecasting at NCEP and the breeding method. *Mon. Wea. Rev.,* **125,** 3297–3319.

Ullman, D. S., P. C. Cornillon, and Z. Shan, 2007: On the characteristics of subtropical fronts in the North Atlantic. *J. Geophys. Res.,* **112,** C01010, doi:10.1029/2006JC003601.